Spontaneous Superlattice Formation in Nanorods through Partial Cation Exchange

Richard D. Robinson[1], Bryce Sadtler[2,†], Denis O. Demchenko[3,†], Can K. Erdonmez[2], Lin-Wang Wang[3], A. Paul Alivisatos[*,1,2]

[1]Materials Science Division, Lawrence Berkeley National Laboratory, Berkeley CA 94720
[2]Department of Chemistry, University of California, Berkeley CA 94720
[3]Computational Research Division, Lawrence Berkeley National Laboratory, Berkeley, CA, 94720

[†] These authors contributed equally to this work
* Corresponding author: alivis@berkeley.edu

Abstract
Lattice mismatch strains are widely known to control nanoscale pattern formation in heteroepitaxy, but such effects have not been exploited in colloidal nanocrystal growth. We demonstrate a colloidal route to synthesizing CdS-Ag_2S nanorod superlattices through partial cation exchange. Strain induces the spontaneous formation of periodic structures. Ab initio calculations of the interfacial energy and modeling of strain energies show that these forces drive the self-organization. The nanorod superlattices exhibit high stability against ripening and phase mixing. These materials are tunable near-infrared emitters with potential applications as nanometer-scale optoelectronic devices.

The ability to pattern on the nanoscale has led to a wide range of advanced artificial materials with controllable quantum energy levels. Structures such as quantum dot arrays and nanowire heterostructures can be fabricated by vacuum and vapor deposition techniques such as molecular beam epitaxy (MBE) and vapor-liquid-solid (VLS), resulting in quantum confined units that are attached to a substrate or embedded in a solid medium (*1-5*). A target of colloidal nanocrystal research is to create these same structures while leveraging the advantages of solution-phase fabrication, such as low-cost synthesis and compatibility in disparate environments (e.g., for use in biological labeling (*6, 7*), and solution-processed light-emitting diodes (*8*) and solar cells (*9*)). One key difference between quantum dots epitaxially grown on a substrate and free-standing colloidal quantum dots is the presence of strain. In epitaxially grown systems, the interface between the substrate crystal and the quantum dot creates a region of strain surrounding the dot. Ingeniously, this local strain has been used to create an energy of interaction between closely spaced dots; this use of "strain engineering" has led, in turn, to quantum dot arrays which are spatially patterned in two (and even three) dimensions (*2-4*). In this paper, we demonstrate the application of strain engineering in a colloidal quantum dot system, by introducing a method that spontaneously creates a regularly spaced arrangement of quantum dots within a colloidal quantum rod.

A linear array of quantum dots within a nanorod effectively creates a one-dimensional (1D) superlattice, a promising new generation of materials (*10, 11*). Such 1D superlattices exhibit confinement effects and are unusual because of their ability to

tolerate large amounts of lattice mismatch without forming dislocations and degrading device performance (*12*, *13*). Strong coupling of electronic states makes them interesting for optical systems and good candidates for photonic applications. 1D superlattices are also of interest for thermoelectric devices and studying ionic transport in 1D systems. VLS growth has demonstrated the formation of extended nanowire superlattices (e.g., alternating Si/Ge or InAs/InP) containing hundreds of repeat units (*14*-*16*). To achieve this, the precursors are alternated for the growth of each layer. The formation of 1D superlattices by this same time-dependent variation of precursor concentration is out of reach for present colloidal growth techniques. The largest number of alternating layers produced so far is three, and yet the sequence of purifications required in that instance were already taxing to implement (*17*).

Cation exchange provides a facile method for systematically varying the proportion of two chemical compositions within a single nanocrystal. We have previously shown that cation exchange can be used to fully (and reversibly) convert CdSe, CdS, and CdTe nanocrystals to the corresponding silver chalcogenide nanocrystal by a complete replacement reaction of the Cd^{2+} cations for Ag^{+} cations (*18*). The resultant material is the silver-anion analog of the starting material (i.e., Ag_2Se, Ag_2S, and Ag_2Te). Size and shape of the nanocrystal is preserved when the nanocrystal has minimum dimensions greater than 4 nm (*18*). The high mobility of cations in the CdS(Se,Te) lattice suggests that partial cation exchange may lead to interesting patterns of segregated domains of silver chalcogenide within a cadmium chalcogenide nanorod. This lead us to investigate the possibility of converting a previously formed nanorod of a

single chemical composition into a striped pattern by a single step partial chemical transformation. In the case explored here, a linear arrangement of regularly spaced Ag_2S dots contained within a CdS rod forms spontaneously at ~36% cation exchange. The near-infrared (NIR) bandgap of the Ag_2S dots is embedded within the larger gap of the CdS, creating a type I heterostructure with interesting optical properties.

Studies of partial cation exchange for 4.8×64 nm CdS to CdS-Ag_2S nanorods are shown in transmission electron microscopy (TEM) images in Figure 1. In these experiments the initial CdS nanorods (Fig. 1A) were exceptionally smooth and the rod diameter was tightly controlled (std. dev. 10%), while the length varied between 30 – 100 nm. The CdS colloidal nanorods were added to a solution of toluene, $AgNO_3$, and methanol at -66 ^{o}C in air (*19*). The concentration of $AgNO_3$ was a controlled fraction of the concentration of Cd^{2+} ions present in the starting material. In the presence of excess Ag^{+}, the rods are completely converted to Ag_2S (*18*). However, when the Ag^{+} ions are limited to yield 36% exchange, the resulting nanorods display a periodic pattern of light and dark-contrast regions (Fig. 1B,C). The average spacing between the dark regions is 13.8 nm with a standard deviation of 28% (Fig. 1 histogram inset). The spacing between periodic segments can be controlled by the diameter of the initial CdS rod (Fig. S1).

Examination of these regions shows that the light and dark-contrast regions are CdS and Ag_2S, respectively. Energy-dispersive x-ray spectroscopy (EDS) indicates that the striped rods alternate between Cd-S and Ag-S rich regions (Fig. 2A) (*20*). Powder x-ray diffraction (XRD) data confirms the presence of wurtzite CdS and monoclinic

Acanthite Ag_2S (Fig. 2B) (*21*). Peaks appearing in the original CdS rods can be indexed to wurtzite CdS (JCPDS #41-1049) and those in the fully exchanged rods can be indexed to Acanthite (JCPDS #14-0072). Peaks visible in the striped rods can be attributed purely to a combination of these two phases. No Ag peaks are present. Furthermore, simulation of the XRD pattern for a mixture of Ag_2S and CdS crystalline domains with dimensions matching the sample's agrees qualitatively with the experimental patterns in terms of relative intensities of Ag_2S peaks to CdS peaks, supporting the extent of the conversion observed in TEM images (Fig. S2). In experimental XRD patterns, the CdS (002) peak is broader and weaker for the striped rods than for the initial CdS sample. This indicates a decreased CdS crystallite size along <001>, the growth axis of the rods (*22*), following the partial ion exchange. Debye-Scherrer analysis of peak widths for several striped rod samples indicates that the CdS grain size along the axis has decreased from >30 nm to 12-16 nm for the striped rods. The decrease in grain size along this direction is attributed to the interruption of the {001} planes by the Ag_2S material, as the shorter length is consistent with the average spacing in this striped rod sample. TEM images show that the Ag_2S regions, which have a broad range of separations at low concentrations (Fig. 3A), become increasingly ordered at slightly higher concentrations (Fig. 1B,C and 3B). The change in the number and periodicity (spacing) of the Ag_2S regions suggest a systematic organization as the volume fraction of Ag_2S increases (Fig. 3C-F). Intra-rod Ag_2S spacings were correlated through a pair distribution function where the distances between each Ag_2S region and all other Ag_2S regions on a rod were measured. Organization of the Ag_2S regions into superlattices is seen in the periodicity of the histogram (Fig. 3F) extending over several nearest neighbor distances. In the

superlattices the Ag_2S regions are spaced evenly along the rod, while no periodicity is seen for the lower Ag^+ concentration (Fig. 3E).

The mechanism by which the initial arrangement of randomly distributed small islands of Ag_2S evolves into a periodic, 1D pattern is of particular interest. Because there exists a positive CdS-Ag_2S interface formation energy (~1.68 eV per Cd-Ag-S elementary interface unit, from our ab initio calculations), it is energetically favorable to merge small Ag_2S islands into larger Ag_2S segments. Fast diffusion of cations leads to a situation where Ostwald ripening between the initially formed islands of Ag_2S can occur, so that larger islands grow at the expense of nearby smaller ones. Diffusion of the cations is allowed as both Ag^+ and Cd^{2+} are considered fast diffusers (*23-25*). Also, silver chalcogenides exhibit superionic conductivity in their high temperature phases (*25*). A critical juncture occurs when the regions of Ag_2S grow to the point where they span the diameter of the rod. At this point, further Ostwald ripening is kinetically prohibited, because an atom-by-atom exchange of Ag^+ among segments will not reduce the total interfacial area. This leads to Ag_2S segments of nearly equal size (Fig. S3). The rod is in a metastable state, i.e., the complete joining of two Ag_2S regions is always a lower energy configuration, but one that cannot readily be accessed by simple atomic exchange events.

A second factor that promotes the regular spacing of the stripe pattern is the elastic repulsion between two Ag_2S segments due to the strain in the intervening CdS region. A model for the coherent atomic connection between the two materials is

depicted in Fig. 4A (*26*). To match the basal lattice constant for CdS (4.3Å), the Ag_2S body centered cubic lattice in the plane of interface has to expand 4% in one direction and contract 15% along the perpendicular direction. There is a repulsive elastic force between segments of like material due to the resulting strain fields. Results from Valence Force Field (VFF) modeling (*27*) found that the elastic energy stored in the rod increases dramatically as two Ag_2S segments approach each other (Fig. 4B). Bond strain in the z-direction (axial) is responsible for the repulsive elastic interaction (Fig. 4C). CdS atoms are pushed away from the closest Ag_2S segment, forming convex shaped atomic layers. For two Ag_2S segments approaching each other, the z-displacements in the CdS are in opposite directions, leading to an interaction term between the fields that gives higher strain energy at smaller separations (*28*). The model is consistent with the experimental finding that increasing the rod diameter increases the spacing between segments (Fig. S1). Similar effects of spontaneous ordering of quantum dots in two dimensions produced by MBE growth have been explained with corresponding arguments (see, for example, Ref. (*3*)). However, the one-dimensional geometry explored here imposes a stronger constraint on ripening processes, leading to an especially robust path to stable, regularly spaced quantum dots within a rod.

The importance of strain in attaining the superlattice pattern can be illustrated by examining similar studies of metal ions reacting with semiconductor nanocrystals. Mokari et. al and Saunders et. al have created interesting new metal-semiconductor nanocrystal heterostructures by reducing Au^{3+} ions onto InAs quantum dots (*29*) and CdS/Se nanorods (*30, 31*). As Au^{3+} has a much greater electron affinity than Ag^{+},

reduction of the ion takes place rather than an exchange reaction. The positive interfacial energy between the two materials drives a phase segregation, similar to our Ag_2S-CdS system, leading to Ostwald ripening. However, epitaxial strain does not play a significant role in the gold growth, and these heterostructures continue to ripen into single metal domains, either at the tip of the (CdS/Se) rod, or inside the quantum dot (InAs). In contrast, the epitaxial relationship between the two phases in the Ag_2S-CdS superlattice structures result in strain fields from the lattice mismatch, which cause like segments to repel each other preventing further ripening.

The resulting striped rods display properties expected of a type I array of Ag_2S quantum dots separated by confining regions of CdS, in agreement with our ab initio calculations of the band structure. The visible CdS photoluminescence (PL) is quenched indicating coupling between materials at the heterojunction (*32*) and near-infrared PL from the Ag_2S segments is observed (Fig. 4D,E). The bandgap of the Ag_2S segments depends upon their size, matching the bulk value (*33*) for fully converted nanorods and shifting to higher energy in smaller dots due to quantum confinement (Fig. 4E). In the present configuration, the Ag_2S quantum dots are only very weakly coupled to each other, because the CdS segments are large. Such structures are of interest for colloidal quantum dot solar cells, where the sparse density of electronic states within a dot may lead to multiple exciton generation (*34*). The formation of nanorod superlattices through partial cation exchange can also be applied to other pairs of semiconductors, yielding a broader class of quantum confined structures. Cation exchange reactions have already been reported in HgS, Ag_2S, SnS_2, CdS, ZnS, Cu_2S, Bi_2S_3 and Sb_2S_3 (*35*-*37*). Two

component combinations of these can produce materials with functional properties ranging from type I (e.g., ZnS – Ag_2S) and type II (e.g., Cu_2S – CdS) band alignments, to thermoelectric power junctions (e.g., CdS – Bi_2S_3).

References

1. S. Guha, A. Madhukar, K. C. Rajikumar, *Applied Physics Letters* **57**, 2110 (1990).
2. M. S. Miller *et al.*, *Journal of Applied Physics* **80**, 3360 (1996).
3. V. A. Shchukin, D. Bimberg, *Reviews of Modern Physics* **71**, 1125 (1999).
4. R. Notzel, *Semiconductor Science and Technology* **11**, 1365 (1996).
5. M. Law, J. Goldberger, P. D. Yang, *Annual Review of Materials Research* **34**, 83 (2004).
6. M. Bruchez, M. Moronne, P. Gin, S. Weiss, A. P. Alivisatos, *Science* **281**, 2013 (1998).
7. W. C. W. Chan, S. M. Nie, *Science* **281**, 2016 (1998).
8. M. Achermann *et al.*, *Nature* **429**, 642 (2004).
9. I. Gur, N. A. Fromer, M. L. Geier, A. P. Alivisatos, *Science* **310**, 462 (2005).
10. D. Y. Li, Y. Wu, R. Fan, P. D. Yang, A. Majumdar, *Applied Physics Letters* **83**, 3186 (2003).
11. M. S. Dresselhaus *et al.*, *Physics of the Solid State* **41**, 679 (1999).
12. G. Kastner, U. Gosele, *Philosophical Magazine* **84**, 3803 (2004).
13. E. Ertekin, P. A. Greaney, D. C. Chrzan, T. D. Sands, *Journal of Applied Physics* **97**, 114325 (2005).
14. Y. Y. Wu, R. Fan, P. D. Yang, *Nano Letters* **2**, 83 (2002).
15. M. S. Gudiksen, L. J. Lauhon, J. Wang, D. C. Smith, C. M. Lieber, *Nature* **415**, 617 (2002).

16. M. T. Bjork *et al.*, *Nano Letters* **2**, 87 (2002).

17. D. J. Milliron *et al.*, *Nature* **430**, 190 (2004).

18. D. H. Son, S. M. Hughes, Y. D. Yin, A. P. Alivisatos, *Science* **306**, 1009 (2004).

19. Materials and methods are available as supporting material on Science Online.

20. A minority of segments are Ag-rich with little or no sulfur, likely due to decomposition of Ag-S compounds by the electron beam (38). This beam damage also distorted the phase and prevented accurate images from being acquired with high-resolution TEM.

21. For these experiments, TEM images show the original CdS rods were 5.3x50 nm, and the striped rods made from these had 5.3x11 nm CdS grains.

22. X. G. Peng *et al.*, *Nature* **404**, 59 (2000).

23. T. D. Dzhafarov, M. Serin, D. Oren, B. Sungu, M. S. Sadigov, *Journal of Physics D-Applied Physics* **32**, L5 (1999).

24. H. H. Woodbury, *Physical Review a-General Physics* **134**, A492 (1964).

25. M. Kobayashi, *Solid State Ionics* **39**, 121 (1990).

26. In both common polymorphs of silver sulfide (cubic and monoclinic), the anion sublattice assumes a body centered cubic structure with only slight distortions in the monoclinic phase (39). Several epitaxial relationships were considered, and the epitaxial connection with minimal lattice distortion to the (001) CdS face is the body centered cubic (110) face (monoclinic (100) face).

27. A. J. Williamson, L. W. Wang, A. Zunger, *Physical Review B* **62**, 12963 (2000).

28. When the segments are very close to each other, however, the elastic energy is actually lowered. With only 3 atomic layers separating the segments (leftmost

point in Fig. 4B) the number of distorted layers in the z-direction is small which results in a smaller repulsive interaction. Additionally, the interaction of the radial distortions from the two segments is cooperative (unlike the z-direction distortions) because they pull the atoms in the same direction. The overall result is a lowering of the elastic energy.

29. T. Mokari, A. Aharoni, I. Popov, U. Banin, *Angewandte Chemie-International Edition* **45**, 8001 (2006).

30. T. Mokari, E. Rothenberg, I. Popov, R. Costi, U. Banin, *Science* **304**, 1787 (2004).

31. A. E. Saunders, I. Popov, U. Banin, *Journal of Physical Chemistry B* **110**, 25421 (2006).

32. D. Battaglia, B. Blackman, X. G. Peng, *Journal of the American Chemical Society* **127**, 10889 (2005).

33. P. Junod, H. Hediger, B. Kilchor, J. Wullschleger, *Philosophical Magazine* **36**, 941 (1977).

34. V. I. Klimov, *Journal of Physical Chemistry B* **110**, 16827 (2006).

35. A. Mews, A. Eychmuller, M. Giersig, D. Schooss, H. Weller, *Journal of Physical Chemistry* **98**, 934 (1994).

36. C. D. Lokhande, V. V. Bhad, S. S. Dhumure, *Journal of Physics D-Applied Physics* **25**, 315 (1992).

37. L. Dloczik, R. Koenenkamp, *Journal of Solid State Electrochemistry* **8**, 142 (2004).

38. L. Motte, J. Urban, *Journal of Physical Chemistry B* **109**, 21499 (2005)

39. H. Schmalzried, *Progress in Solid State Chemistry* **13**, 119 (1980)

40. This work was supported by the U.S. Department of Energy under the contract number DE-AC02-05CH11231. We would like to thank Chris Nelson, Christian Kisielowski, and the National Center for Electron Microscopy at Lawrence Berkeley National Lab. We also thank Dmitri Talapin, Tim Teague, and Dong-Hee Son. R.D.R. thanks the Lawrence Berkeley National Laboratory for the Lawrence Postdoctoral Fellowship.

Supporting Online Material
www.sciencemag.org
Materials and methods
Supporting Online Text
Figures S1, S2, S3

Figure captions

Figure 1. TEM images of superlattices formed through partial cation exchange. (A) The original 4.8×64 nm CdS nanorods. (B,C) Transformed CdS-Ag_2S superlattices. Inset to (C) is a histogram of Ag_2S segment spacing (center-to-center). Average spacing is 13.8 ± 3.8 nm. The sample set for the histogram was greater than 250 nanorods.

Figure 2. Characterization of CdS-Ag_2S heterostructures. (A) EDS spectra of the striped rods at the light (top) and dark (bottom) contrast regions, corresponding to Cd-S and Ag-S rich regions. (B) XRD spectra of CdS rods (black line), superlattices (blue line), and fully exchanged Ag_2S rods (green line). Spectra from the striped rods show new peaks corresponding to Ag_2S, and a modified (002) peak, indicating interruption of the CdS lattice along the rod axis.

Figure 3. Effects of increasing $AgNO_3$ concentration. TEM images: (A) Low concentration (Ag^+/Cd^{2+} ~0.2). (B) Intermediate concentration that produce the nanorod superlattices (Ag^+/Cd^{2+} ~0.9). Scale bar is 20 nm. Histograms of the number of Ag_2S regions per rod: (C) Low concentration and (D) intermediate concentration. More than 250 nanorods were examined for each histogram. Pair distribution histograms for Ag_2S regions on individual CdS-Ag_2S nanorods: (E) Low concentration and (F) intermediate concentration. Intra-rod distances between each Ag_2S region, measured for 200 nanorods in each of the sample sets shown in (A) and (B). Spacings were normalized by the number of Ag_2S regions and the length of the rod. Low concentration (E) shows no

correlation beyond the nearest neighbor spacing. Intermediate concentration (F) shows a periodicity, which extends over several nearest neighbors.

Figure 4. Theoretical modeling and experimental optical characterization. (A) Cubic-cutout representation of cells used for ab initio energy calculations. Distorted monoclinic Ag_2S (100) plane connects with the wurtzite CdS (001) plane. (B) Elastic energy of rod as a function of segment separation (center-to-center). (C) Z-axis strain for the case of two mismatched segments at a center-to-center separation distance of 14.1 nm (top) and 12.1 nm (bottom). Elastic interaction between segments is greatly reduced for separations > 12.1 nm. Arrows show placement of mismatched segments. CdS rods used for VFF calculations (B,C) were 4.8 nm diameter with two 4.8×4.0 nm lattice-mismatched segments. Effective elastic constants for the mismatched segments were from ab initio calculations for monoclinic Ag_2S. (D) Visible and (E) NIR PL spectra at λ = 400 and 550 nm excitation, respectively. Coupling between the CdS and Ag_2S is evident by the complete quenching of the visible PL (D) in the heterostructures. The shift in NIR PL (E) is due to quantum confinement of the Ag_2S.

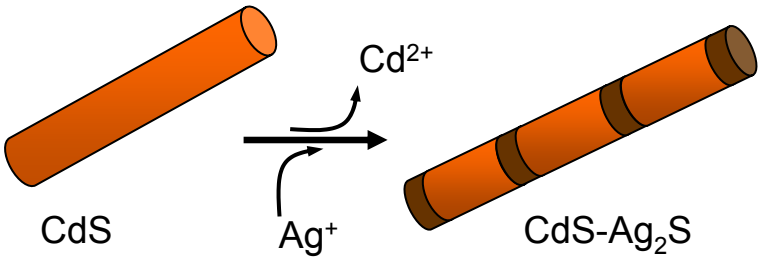
Cd2+
CdS
Ag+
CdS-Ag2S

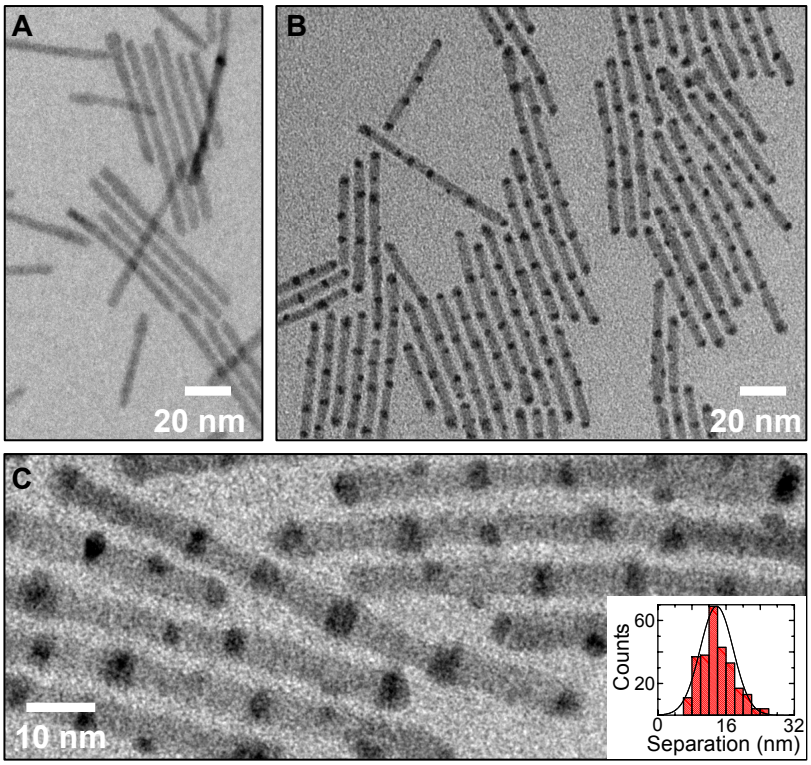
A
20 nm
B
20 nm
C
10 nm
Counts
60
20
0
16
32
Separation (nm)

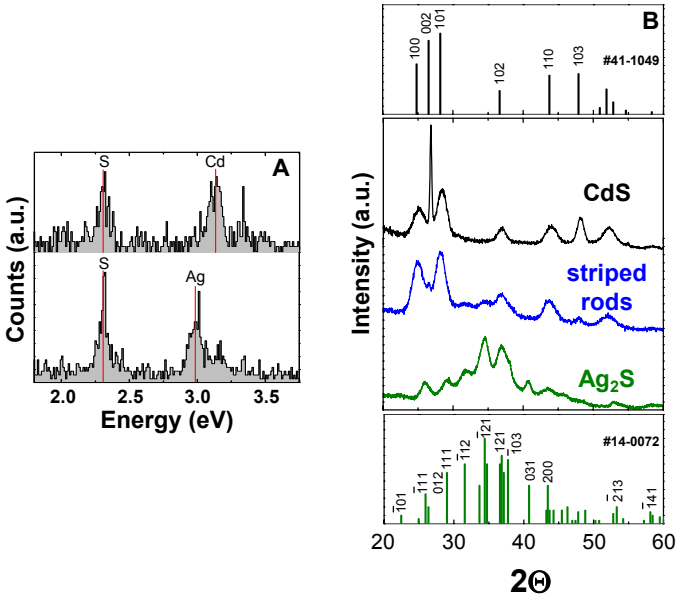
A
S
Cd
S
Ag
Counts (a.u.)
2.0
2.5
3.0
3.5
Energy (eV)
B
100
002
101
102
110
103
#41-1049
CdS
striped
rods
Ag2S
#14-0072
101
111
012
111
112
121
121
103
031
200
213
141
Intensity (a.u.)
20
30
40
50
60
2Θ

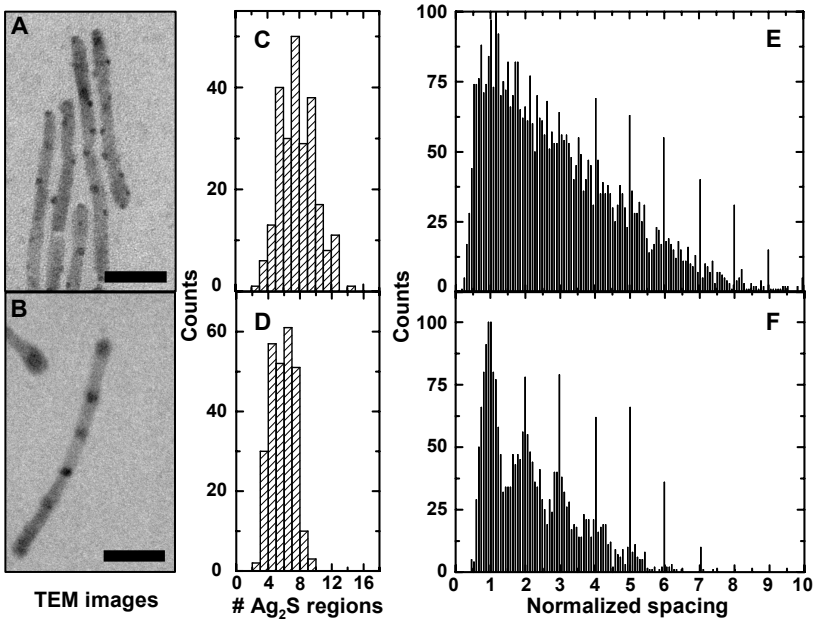
A
B
TEM images
C
D
Counts
Ag2S regions
E
F
Counts
Normalized spacing

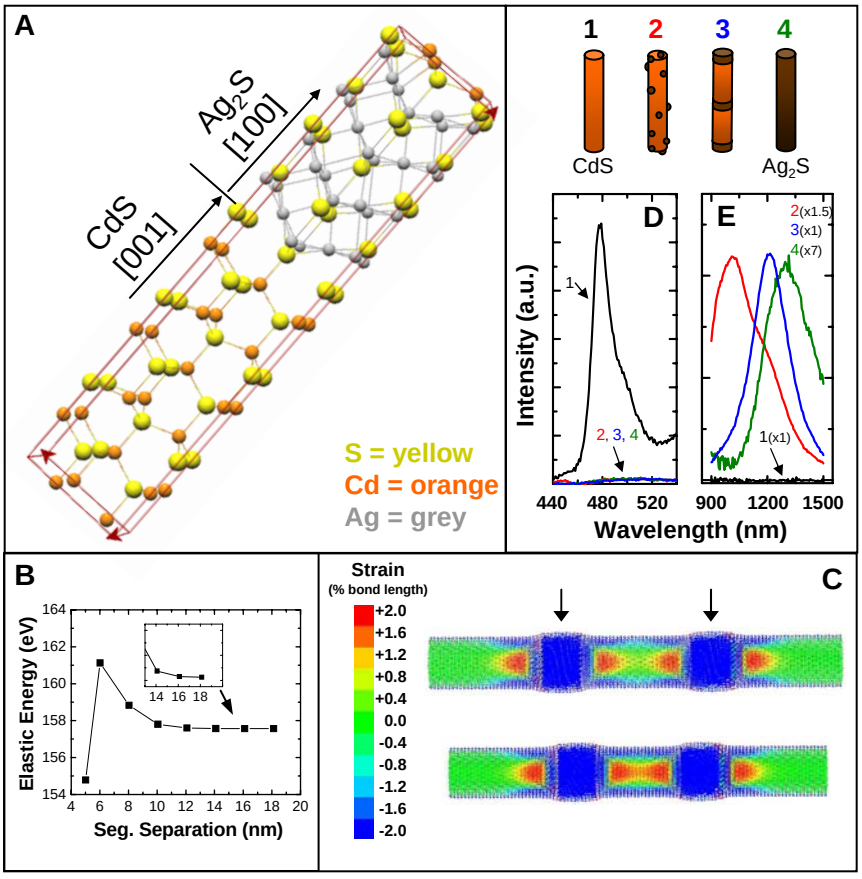
A
Ag2S
[100]
CdS
[001]
S = yellow
Cd = orange
Ag = grey
1
2
3
4
CdS
Ag2S
D
E
Intensity (a.u.)
1
2, 3, 4
2(x1.5)
3(x1)
4(x7)
1(x1)
440 480 520
900 1200 1500
Wavelength (nm)
B
Elastic Energy (eV)
164
162
160
158
156
154
14 16 18
4 6 8 10 12 14 16 18 20
Seg. Separation (nm)
Strain
(% bond length)
+2.0
+1.6
+1.2
+0.8
+0.4
0.0
-0.4
-0.8
-1.2
-1.6
-2.0
C

Supporting Online Material
Materials, methods and supporting online text
Figures S1, S2, S3

Chemicals. Cadmium oxide (CdO, 99.99%), silver nitrate ($AgNO_3$, 99+%), sulfur (99.99%), toluene (99%), and nonanoic acid (96%) were purchased from Aldrich. Isopropanol was purchased from Fisher Scientific and methanol was purchased from Fisher Scientific or EMD Chemicals. Tetradecylphosphonic acid (TDPA) and octadecylphosphonic acid (ODPA) were purchased from Polycarbon Industries (PCI Synthesis, 9 Opportunity Way, Newburyport, MA 01950, 978-463-4853). Trioctylphosphine oxide (TOPO, 99%) was purchased from Acros Organics. Tetrachloroethylene was obtained from Kodak. Trioctylphosphine (TOP, 97%) was purchased from Strem Chemicals. Trioctylphosphine sulfide (TOPS) was prepared by mixing TOP and sulfur together in a 1:1 molar ratio in a glovebox followed by stirring at room temperature for >36 hours.

Synthesis of CdS nanorods. Two CdS rod samples were used for the cation exchange reactions in the data reported here. The CdS nanorod dimensions were 4.8±0.5 × 64±17.6 nm (sample A) and 5.3±0.4 × 50±10.5 nm (sample B). The reactions were performed using standard Schlenk line techniques. For both reactions 210 mg of CdO and 2.75 g of TOPO were placed in a 25 ml, 3-neck flask. For sample A, 1.06 g of ODPA was added to the flask and for sample B, 0.80 g of ODPA and 0.22 g of TDPA was used. The contents of each flask were evacuated at 120ºC for > 30 minutes, and then the flasks were heated to 320ºC under argon for 15 minutes to allow the complexation of cadmium

with phosphonic acid. The reaction mixtures were cooled to 120ºC and again evacuated for 1 hour to remove water produced during the complexation. While heating back up to 320ºC, 2 g of TOP was injected into each flask. Then TOPS was injected (1.95 g for sample A and 1.3 g for sample B) and the nanocrystals were grown for 85 minutes at 315ºC. After cooling, toluene was added to the reaction mixtures, and the nanocrystal solutions were opened to air. The nanorods were washed several times by adding equal amounts of nonanoic acid and isopropanol -- to induce flocculation -- followed by centrifugation to precipitate the CdS nanorods. The supernatant was removed, and the precipitated nanorods were redispersed in fresh toluene. This reaction produces some branched structures (i.e., bipods, tripods, and tetrapods) along with the rods. However, these are removed during the washing, as the branched CdS structures do not flocculate as easily as the rods and thus stay in the supernatant.

Cation exchange of CdS nanorods. CdS nanorods in toluene were added to a solution of toluene, $AgNO_3$, and methanol at -66 ^oC in air. The reaction vials were capped after adding the CdS nanorod solution and allowed to warm to room temperature for a period of at least 30 minutes. The amounts used for a typical reaction to produce the CdS-Ag_2S superlattices were 2.0 ml of toluene, 0.6 ml of a 1.2×10^{-3} M $AgNO_3$ solution in methanol, 0.3 ml methanol, and 0.2 ml of CdS particles in toluene (OD ~0.8 at λ = 350 nm for 2.2 ml). The approximate ratio of Ag^+/Cd^{2+} to produce structures 1-4 depicted in Figure 4 are 0, 0.14, 0.80, and 8.00. These structures were: 1 (CdS rods, Sample B), 2 (small Ag_2S islands on CdS rods), 3 (CdS-Ag_2S superlattices), and 4 (Ag_2S rods).

Characterization:

Transmission electron microscopy (TEM) was carried out on an FEI Technai G^2 20 Supertwin, operating at an accelerating voltage of 200 kV. The filament was LaB6.

The statistics for the length and diameter of the original CdS nanorods as well as number of Ag_2S regions per rod, center-to-center spacing, and segment lengths of the Ag_2S regions in the CdS-Ag_2S nanorod heterostructures were determined from TEM images (taken at a magnification of 97,000× to 195,000×) using Image-Pro Plus software, and making at least 250 measurements. Some superlattices contained small Ag_2S islands on the surface of the nanorod whose diameter was less than 25% of the CdS rod diameter; these islands were disregarded in the spacing measurements. Gaussian functions were used to fit the histograms. Averages and standard deviations were calculated directly from the raw data.

For the pair distribution histograms, coordinate markers were placed on the Ag_2S regions of the CdS-Ag_2S nanorod heterostructures using Image-Pro Plus software on TEM images taken at a magnification of 97,000x to 195,000x. For the partially formed Ag_2S segments (which are the majority in the low Ag^+ case, Figure 3A, and are a small fraction in the intermediate Ag^+ case, Figure 3B), the marker was placed at the center of the rod rather than the center of the Ag_2S region so that only the distance component parallel to the rod axis between Ag_2S segments is measured. This avoids error in measurement due to the 2D representation (TEM image) of a 3D object (in this case a cylindrical rod). The

coordinates were then used to compute the distance between each Ag_2S region on a CdS rod with all other Ag_2S regions on that rod. These pair wise distances were measured for over 200 nanorods, to generate the histograms shown in Figure 3. The spacings were normalized by multiplying by (n-1)/L (where n = the number of Ag_2S regions and L = sum of nearest neighbor spacings on the rod). As an Ag_2S region was found to always occur at each end of the rod, L is approximately the rod length. The bin size of the histogram was chosen as 0.07.

To estimate the volume fraction of the superlattices, the length fraction of Ag_2S segments within the superlattices was measured from TEM images for 40 nanorod superlattices. Assuming the diameters of all the segments are equal, the volume fraction is proportional to the length fraction. This gives a volume fraction of ~36 % Ag_2S, which is a slightly lower value than if 100% of the Ag^+ added had exchanged to form Ag_2S within the rods.

Energy-dispersive X-ray spectroscopy (EDS) was collected on a Philips CM200/FEG STEM equipped with an ultra-thin window silicon EDS detector from Oxford, at the National Center for Electron Microscopy at Lawrence Berkeley National Laboratory. Spherical aberration (Cs) and chromatic aberration (Cc) were both 1.2 mm. An operating voltage of 200 kV was used with an energy dispersive x-ray detector having energy resolution of 136 eV for Mn-Kα radiation (136 eV FWHM at 5.895 keV Mn-Kα).

Powder X-ray diffraction (XRD) was taken on a PANalytical X'Pert PRO MPD with an X'Celerator detector and a copper (Cu-Kα) radiation source (1.542 Å) operating at 40 kV and 40 mA. The accumulation time for each sample was at least 4 hours with a step size of 0.0334 degrees. XRD samples were prepared by depositing a precipitated sample on a silicon plate or centrifuging the sample into a 0.3 mm Borosilicate capillary.

Fluorescence spectra were recorded on a HORIBA Jobin Yvon Fluorolog 3 equipped with a Triax 320 spectrometer at the Molecular Foundry at Lawrence Berkeley National Laboratory. The nanocrystals were precipitated and redispersed in tetrachloroethylene for the measurements. For spectra in the visible range, the excitation wavelength was 400 nm, and a photomultiplier tube (PMT) was used for detection. For the near-infrared region, the excitation wavelength was 550 nm, and a liquid nitrogen cooled InGaAs photodiode detector was used. When taking the near infrared spectra, a long-pass filter with a cutoff of 650 nm was placed in front of the detector to prevent aliasing of the excitation wavelength. The emission spectra were corrected for the wavelength-dependent response of the emission grating and detector and the background of the solvent.

For the data that appears in this manuscript, TEM images (Fig. 1,3) and accompanying histograms, EDS measurements (Fig. 2A), and Ag_2S segment lengths (Fig. S3) were from structures made from sample A CdS. XRD spectra (Fig. 2B, S2) and optical measurements (Fig. 4D,E) were from structures made from sample B CdS. Both samples appear in diameter comparison histograms (Fig. S1).

Ab inito modeling:

The ab initio calculations of the electronic structure of Ag_2S and CdS were performed using Vienna Ab-initio Simulation Package (VASP) (S*1*) and Parallel total Energy (PEtot) (S*2*) programs, utilizing the local density approximation (LDA) and generalized gradient approximation (GGA) to the density functional theory (DFT). We used norm-conserving pseudopotentials in order to model the electron-ion interaction (in PEtot) as well as projector-augmented wave (PAW) method (in VASP). Planewave basis sets are used with kinetic energy cutoffs ranging from 20 to 75 Ry, with Monkhorst-Pack k-point meshes to sample the Brillouin zone (up to 256 reducible points). These techniques were used to estimate stability of various Ag_2S phases, find the optimal geometry for the epitaxial attachment, calculate the formations energies of the CdS-Ag_2S interfaces, and calculate the corresponding band alignment. For the interface calculations the supercells were constructed containing 20 S, 12 Cd, and 16 Ag atoms, with their positions fully relaxed using ab initio forces. The band alignment was estimated by comparing the site-projected densities of states (DOS) of the most bulk-like S atoms in the supercell (in Ag_2S and CdS slabs) with the site-projected DOS of the bulk Ag_2S and CdS. The shift in valence band DOS from their bulk values is then equal to the valence band alignment for the interface. The conduction band alignment is obtained by adding the bulk experimental band gap value to the valence band energy in order to overcome the known tendency of the LDA/GGA to underestimate the value of the band gap.

The elastic constants of the Ag_2S bulk crystal were also estimated using the ab initio methods outlined above. The elastic constants C_{ij} were computed by distorting the crystal in corresponding directions and fitting the total energy into the second order elastic expansions.

VFF modeling:

Elastic energies and strains were estimated using the Valence Force Field (VFF) method, which is an atomistic bond stretching and bending model. The VFF model parameters for CdS are available in the literature, while the parameters for the experimentally observed Ag_2S phase were obtained by fitting the elastic constants of Ag_2S obtained from the ab initio calculations into the VFF. A CdS nanorod was constructed to have two inclusion segments of a different material with a lattice mismatch and the elastic constants corresponding to the CdS-Ag_2S nanorod superlattice. All the atomic positions were relaxed according to the VFF model, and the elastic energy after the relaxation was calculated. This was done for several segment-segment separation distances. The nanorod diameter was 4.8 nm.

To understand the repulsive elastic energy it is necessary to understand that the VFF model relaxes atoms in all directions. In a simplified 1D model there would be no interaction energy between two islands; each island would add elastic energy based solely on the distance from the interface regardless of the strain induced by the other. For a single segment, the elastic strain field decays roughly exponentially from the interface as $\sim\exp[-x/(\beta d)]$, where x is the distance from the interface measured along the length of the

rod, d is the nanorod diameter, and β is a constant (S*3*). The elastic energy is proportional to the square of the elastic strain field, but the force is a derivative of the energy, leaving a linear relation between the force and strain created by an island. Calculations show that no higher order terms occur in the energy expression. If another segment were to apply a strain near the first segment the two forces would add directly, as if each were acting independently. Thus there is no interaction between the islands from a 1D perspective. However, since the VFF modeling is 3D, atomic movements in the other spatial directions exhibit considerable influence on the overall energy, creating the interaction terms that lead to higher energy as the inclusion segments approach each other.

XRD simulation:

The powder patterns expected from a mixture of short CdS (5.3×11 nm; wurtzite, JCPDS #41-1049) rods and Ag_2S nanocubes (edge length = 5.0 nm; monoclinic, Acanthite JCPDS #14-0072) was simulated. Those domain sizes were chosen to mimic the approximate volumes and shapes seen in TEM images for alternating CdS and Ag_2S domains. The simulated patterns provide a reference for the experimental nanorod superlattice patterns obtained.

For each of the two nanocrystalline domains under consideration, the computation proceeds as follows. Given the desired shape and crystal phase, the Cartesian positions of atoms constituting the nanocrystal was calculated. (No defects/strain were allowed for in the calculations.) The atomic positions were used to calculate a list of all pairwise

interatomic distances (r_{ij}, with i and j denoting i-th and j-th atoms). This list on its own is sufficient for an exact calculation of the powder pattern (S*4*). For computational efficiency, however, the list of distances was binned into a histogram. Then, an extension of the below approximate expression yields the expected powder XRD intensity profile,

$$I(S)\alpha \frac{F^2(S)}{S}\sum_{k}^{N}\frac{p_k}{r_k}\sin(2\pi r_k S)$$

where $S = 2\sin(\theta)/\lambda$ is the scattering parameter, *I(S)* is the observed intensity, r_k is the value of r at center of a 'bin' and p_k is the number of occurrences of interatomic distances falling within the bin centered around r_k (S*5,* S*6*). *N* is the total number of bins. *F(S)* is the atomic structure factor, in our case, of cadmium, silver, and sulfur. The bin widths are small enough that the simulated pattern is insensitive to further decrease of the bin width (~0.001 Å). Note that the expression given above is a simple form that applies to particles made of only one chemical species. For our multi-species particles, we used a straightforward extension with *F(S)* being replaced in the correct expression by three different appropriate atomic structure factors, in our case, of cadmium, silver, and sulfur.

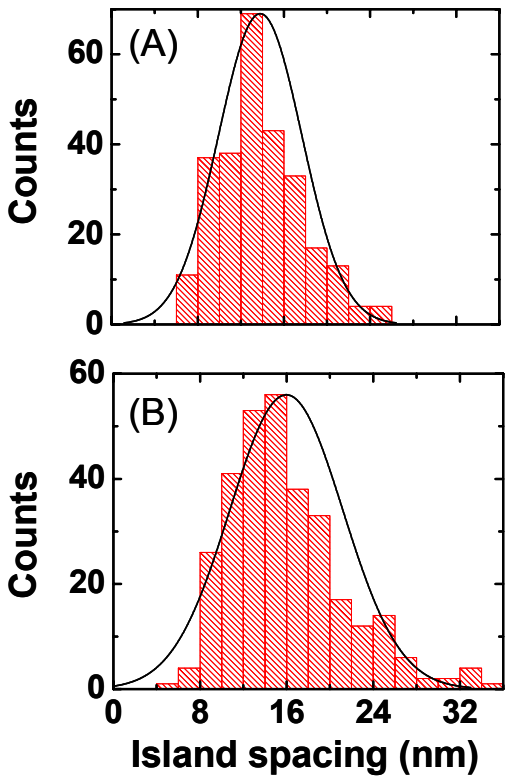

Figure S1. Diameter dependence of Ag_2S segment spacing. (A) 4.8 nm diameter CdS rods and (B) 5.3 nm diameter CdS rods. Superlattices were made from two different CdS substrates, one with 4.8 nm diameter nanorods and the other with 5.3 nm diameter nanorods. Spacing increases with rod diameter from 13.8 nm for the 4.8 nm diameter rods to 16.0 nm for the 5.3 nm diameter rods. Center-to-center distance was used to determine spacing. More than 250 rods were measured for each histogram.

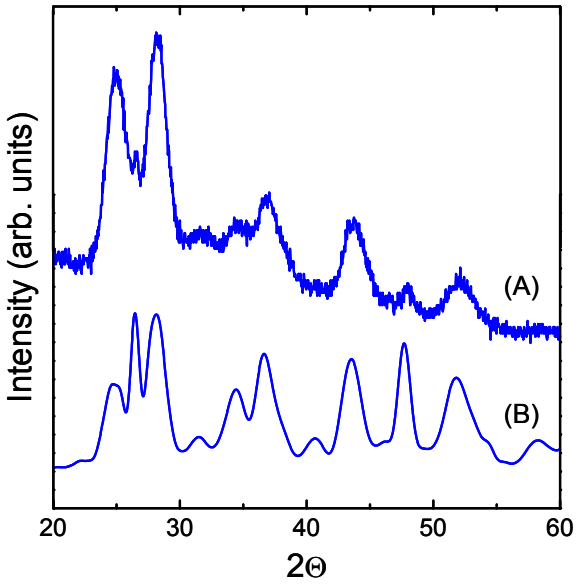

Figure S2. Comparison of XRD spectra from (A) nanorod superlattice experiments and (B) numerical simulation. Experimental data is same as in Figure 2. Simulation is a sum of patterns expected for 5.3×11 nm CdS rods and 5.0 nm Ag_2S cubes. (This is equivalent to an Ag_2S center-to-center spacing of 16 nm.) The simulation spectrum qualitatively matches the experimental spectrum; the Ag_2S peaks at ~32° and 34° and the broadened shoulder at ~39° are evident in both the simulated and experimental spectra.
Ag_2S peaks appear slightly broader and thus less distinct in the experimental pattern. We attribute this to the (expected) significant strains in the Ag_2S segments that the simulations do not take into account. Another difference between theoretical and experimental profiles is the lower intensity of the CdS (002) and (103) peaks in the experimental patterns. The weaker than ideal (103) peak is readily explained by the presence of stacking faults in the wurtzite CdS phase. The low (002) intensity is harder to explain; presently, we believe it to be due to non-random alignment of rods on the sample substrate.
For these experiments, TEM images show the original CdS rods were 5.3x50 nm, and the striped rods made from these had 5.3x11 nm CdS grains.

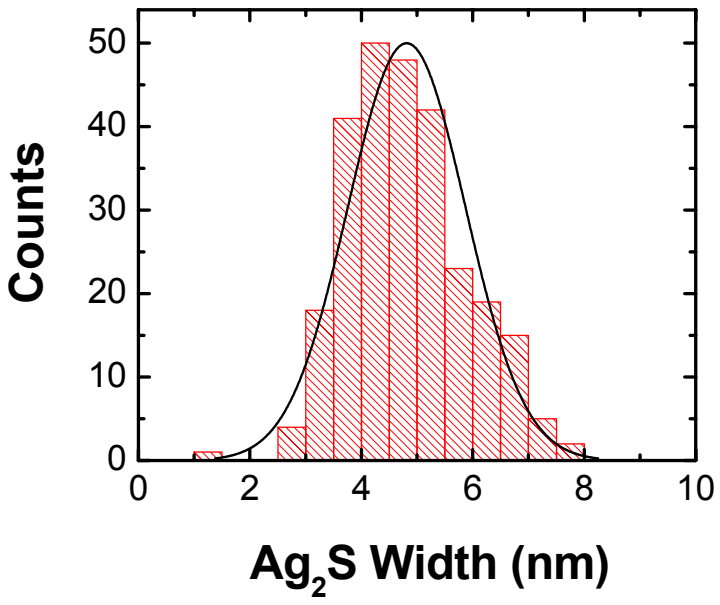

Figure S3. Histogram of Ag_2S segment lengths (measured along the rod-axis) for the nanorod superlattices shown in Figure 1. Average width = 4.8 nm, standard dev. = 22%. More than 250 rods were measured.

References

S1. G. Kresse, J. Furthmuller, *Computational Materials Science* **6**, 15 (1996).

S2. http://hpcrd.lbl.gov/~linwang/PEtot/PEtot.html

S3. E. Ertekin, P. A. Greaney, D. C. Chrzan, T. D. Sands, *Journal of Applied Physics* **97**, 114325 (2005).

S4. A. Guinier, *X-ray diffraction in crystals, imperfect crystals, and amorphous bodies* (W.H. Freeman, San Francisco, 1963).

S5. B. D. Hall, R. Monot, *Computers in Physics* **5**, 414 (1991).

S6. J. N. Wickham, A. B. Herhold, A. P. Alivisatos, *Physical Review Letters* **84**, 923 (2000).